


## Article

# Effects of Preparation Conditions on the Efficiency of Visible-Light-Driven Hydrogen Generation Based on Cd<sub>0.25</sub>Zn<sub>0.75</sub>S Photocatalysts

Maali-Amel Mersel <sup>1</sup>, Lajos Fodor <sup>1</sup>, Péter Pekker <sup>2</sup>, Miklós Jakab <sup>3</sup>, Éva Makó <sup>3</sup> and Ottó Horváth <sup>1,\*</sup> 

<sup>1</sup> Research Group of Environmental and Inorganic Photochemistry, Center for Natural Sciences, Faculty of Engineering, University of Pannonia, P.O.B. 1158, H-8210 Veszprem, Hungary; sam003miloo@gmail.com (M.-A.M.); lajos@almos.uni-pannon.hu (L.F.)

<sup>2</sup> Environmental Mineralogy Research Group, Research Institute of Biomolecular and Chemical Engineering, University of Pannonia, P.O.B. 1158, H-8210 Veszprem, Hungary; pekkerpeter@gmail.com

<sup>3</sup> Research Center for Engineering Sciences, Department of Materials Engineering, University of Pannonia, P.O.B. 1158, H-8210 Veszprem, Hungary; jakab.miklos@mk.uni-pannon.hu (M.J.); makoe@almos.uni-pannon.hu (É.M.)

\* Correspondence: horvath.otto@mk.uni-pannon.hu; Tel.: +36-88-624-000 (ext. 6049)

**Abstract:** Photocatalytic H<sub>2</sub> production utilizing H<sub>2</sub>S, an industrial side-product, is regarded as an environmentally friendly process to produce clean energy through direct solar energy conversion. For this purpose, sulfide-based materials, such as photocatalysts, have been widely used due to their good solar response and high photocatalytic activity. In this work, a ZnS–CdS composite was studied, and special attention was dedicated to the influence of the preparation parameters on its H<sub>2</sub> production activity. The ZnS–CdS composite, with an enhanced photoactivity for H<sub>2</sub> production, was synthesized both from ammine complexes and, in a conventional way, directly from acetates at various pH values. Deviating from the traditional method, the photoactivity of ZnS–CdS prepared from ammine complexes was not affected by the pH. Besides, the hydrothermal treatment and the ammonia content strongly influenced the rate of H<sub>2</sub> production in this system. DRS, TEM, SEM, XRD, and quantum yield measurements prove the dependence of the photoactivity of these catalysts on the structural and morphological properties determined by the preparation conditions. The promising photocatalytic efficiency achieved with the application of these ZnS–CdS catalysts, prepared without any metal deposition, encourages further investigations to enhance the rate of hydrogen generation by optimization of the reaction conditions for practical utilization.

**Keywords:** photocatalysis; hydrogen generation; visible-light-driven; solar energy conversion; ZnS–CdS composite; preparation conditions



**Citation:** Mersel, M.-A.; Fodor, L.; Pekker, P.; Jakab, M.; Makó, É.; Horváth, O. Effects of Preparation Conditions on the Efficiency of Visible-Light-Driven Hydrogen Generation Based on Cd<sub>0.25</sub>Zn<sub>0.75</sub>S Photocatalysts. *Catalysts* **2021**, *11*, 1534. <https://doi.org/10.3390/catal11121534>

Academic Editors: Weilin Dai and Trong-On Do

Received: 3 November 2021

Accepted: 10 December 2021

Published: 16 December 2021

**Publisher's Note:** MDPI stays neutral with regard to jurisdictional claims in published maps and institutional affiliations.



**Copyright:** © 2021 by the authors. Licensee MDPI, Basel, Switzerland. This article is an open access article distributed under the terms and conditions of the Creative Commons Attribution (CC BY) license (<https://creativecommons.org/licenses/by/4.0/>).

## 1. Introduction

Nowadays, the main atmospheric issues arise from the increased consumption of fossil fuels, urging the development of an alternative source of energy to meet the world's energy demand [1]. Therefore, hydrogen, as a clean and environmentally friendly energy source, was considered to be the most promising candidate, especially after Fujishima and Honda demonstrated photocatalytic hydrogen production by decomposition of water, using semiconductor materials in the early seventies [2,3]. Photocatalytic hydrogen evolution via water splitting remains an important research topic, as indicated by the review of Zhang et al. [4]. The decomposition of H<sub>2</sub>S instead of H<sub>2</sub>O was widely investigated and shown to be economically and environmentally improved, because it required less energy and resulted in the removal of H<sub>2</sub>S, an extremely toxic gas that is mainly produced from the refinery of crude oil and contributes to acid rain [5].

The most common type of photocatalysts previously used were metal oxides [6,7] such as NiO/Ta<sub>2</sub>O<sub>5</sub>K [8], ZnO/TiO<sub>2</sub> [9], Au/ZnO [10], ZnO/Fe<sub>2</sub>O<sub>3</sub> [11]. These materials mostly

utilized ultraviolet radiation, which only represents a small part of the solar spectrum. Sulfide-based semiconductors exhibit a better solar response than oxides and have highly negative potential conduction bands suitable for H<sub>2</sub>O reduction. Hence, numerous recent studies have focused on the development of these types of photocatalysts. The main sulfide-based catalysts have been reviewed by Zhang and Guo; most of them consist of block d transition metals with d<sup>10</sup> electron configuration, and the most investigated type was CdS or ZnS–CdS [12]. ZnS possesses a highly negative conduction band position, making it possible to achieve a higher efficiency without requiring modification; on the other hand, CdS has a good solar response due to its narrow band gap. The ZnS–CdS composite belongs to the heterojunction photocatalysts which provide an improved separation of the photogenerated electron-hole pairs, resulting higher efficiency [4]. Additionally, the stabilization and immobilization of ZnS–CdS nanoparticles were realized by the application of polyphosphate, gelatin, polyvinyl alcohol [13], or polystyrene [14]. The Fe<sub>2</sub>O<sub>3</sub>/ZnS–CdS core–shell nanoparticles were prepared for this purpose [15].

A variety of articles have previously reported the excellent photoactivity of the ZnS–CdS semiconductor and how it could be increased by metal modification [16–21], however, only few have taken in account the preparation method and the initial parameters and how they may affect the rate of hydrogen production. A simple precipitation of ZnS–CdS from acetate or nitrate salts with Na<sub>2</sub>S or TAA (thioacetamide) was applied in most cases with [18,22–24] or without further hydrothermal treatment (HTT) [14–16,25,26]. In some cases, other sulphide sources were used, such as Na<sub>2</sub>S<sub>2</sub>O<sub>3</sub> [27], thiourea [28–30], cysteine [31] or xanthate [32].

According to Gonzalez-Panzo, I.J. et al. [33], CdS's precipitation is more favorable at pH > 10 and that of ZnS at pH > 11.5, which suggests that preparing the catalyst with the usual direct precipitation method would lead to a core–shell structure (CdS coated with ZnS), while preparation from ammine complexes could ensure the simultaneous precipitation of ZnS and CdS because the initial pH is increased to approximately 13. Guo and co-workers applied an ethylenediamine complexing agent for the preparation of the ZnS–CdS composites using TAA as a sulphide source [21,34,35]. They achieved considerably high quantum yields by this method. In the present work, a comparison between the conventional preparation method and the synthesis applying ammine complexes was made. The effects of other parameters and conditions such as pH, concentrations, hydrothermal treatment, and the order of the preparation steps (i.e., mixing order) on the structure and the efficiency of the catalyst were also investigated.

## 2. Results and Discussion

### 2.1. The Effect of the Mixing Order

In the literature, two different orders for the mixing of the reactants can be found regarding the preparation of the photocatalysts used in this work. Generally, the sulfide reagent was added to the solution containing the metal ions (designated as “normal order”), but in some cases a reverse order was applied [20,36]. Therefore, the effect of the mixing order of the reagents was investigated with regard to the photoactivity of the catalysts.

In this paper, we depicted the rate of hydrogen production (RHP) as a function of the illumination time, but in the bar diagrams, its average calculated for the 200–400 min time range is represented. RHP is provided by μmol H<sub>2</sub> evolved during one hour (i.e., the unit of measurement is μmol/h). The temperature of the collected hydrogen was the same for each experiment (22 °C), we used the same light source and geometrical arrangement for all irradiations in this work. Hence, RHP is linearly proportional to the quantum yield of the hydrogen production.

Two catalysts containing CdS and ZnS in 1:3 molar ratio were prepared. Each of the preparation conditions was the same except for the mixing order of the reagent solutions. The catalyst prepared by the “normal order” (i.e., when the Na<sub>2</sub>S solution was added to the solution containing the metal ions) resulted in more than 25% higher RHP compared to that of the one prepared by the reverse order (when the solution of ammine complexes was

added to the sulfide solution) (Figure 1). Since there was a significant difference between the two catalysts, the “normal order” was applied for further preparations.

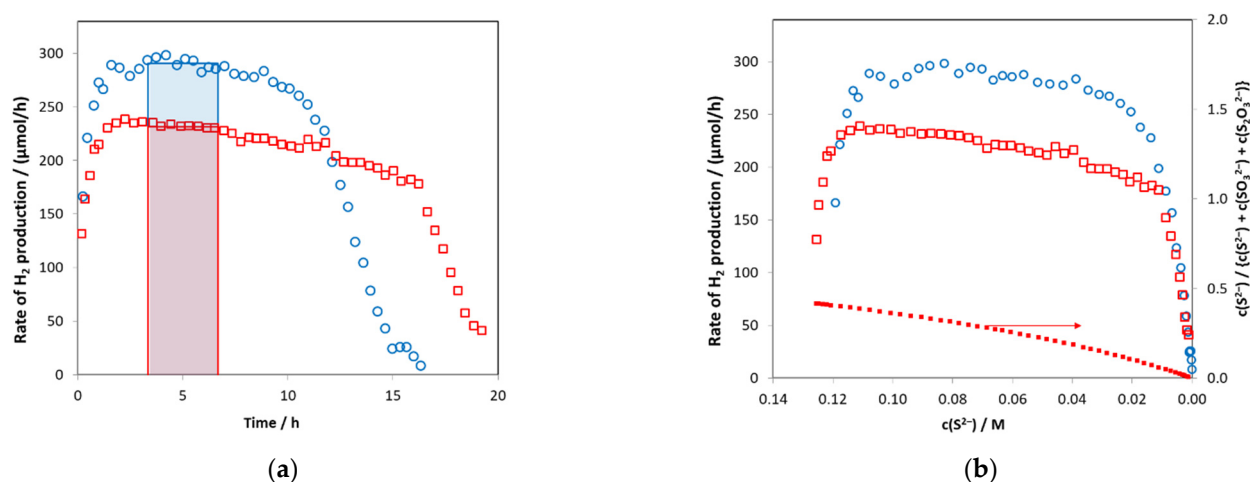


**Figure 1.** The rate of H<sub>2</sub> production as a function of time (a) and sulfide concentration (b). The red square and the blue circle symbols represent the rate for catalyst prepared in reverse and normal order, respectively (see in the text). The bars in Figure 1a. shows the average rate calculated for the 200–400 min time region. The small filled squares gives the ratio of sulfide concentration to the total concentration of all sulfur containing anions.

The shape of the rate functions shown in Figure 1a is similar to those obtained for the other catalysts tested. After an initial increase, it shows a slow decrease, then, close to the end of the reaction, it steeply decreases until the sulfide ions are completely consumed. In order to better understand the changes, the rates (RHP values) were also plotted as a function of the sulfide concentration (Figure 1b). The concentration of sulfide was calculated as described in our previous article [37]. Liu and colleagues previously found that RHP displays first-order kinetics regarding the sulfide ions [38]. In the case of the catalysts studied in this work, it can be clearly seen that only at sulfide concentrations of less than 0.01 M (at the end of the reaction) was a direct proportionality between the rate and  $c(S^{2-})$  observed. The reaction rate was almost constant during most of the irradiation, as it only slightly decreased, and the slope of this decrease is significantly less than that of the decrease of the sulfide concentration. At this stage, the reaction is diffusion-controlled with pseudo-zero-order kinetics. To interpret this change, it is worth comparing this with the initial increase as well as with the publications describing that the thio functional groups on the surface of CdS and ZnS crystals produced from aqueous media are partially replaced by oxo or hydroxo groups [18,38]. On this basis, it is likely that, in the reaction leading to equilibrium at the initial stage of illumination, the oxo/hydroxo surface function groups will be replaced with sulfide, which will cause an initial increase of the rate. (Notably, at the beginning of the irradiation, the temperature also increases from 25 °C to about 40 °C, but this temperature is reached in less than 1 h, while the increase in the rate often last for 3–4 h.) A slight decrease in the middle stage of the reaction is likely to be a combined effect of several factors. One of the reasons is that sulfide ions must first adsorb onto the catalyst surface to react with the photogenerated hole, but in this process they compete with other ions in the solution. Since the concentration of sulfide decreases in the photoinduced process, while that of thiosulfate increases, the ratio of sulfide concentration to that of other sulfur-containing anions decreases (Figure 1b), which inhibits the adsorption of sulfide ions onto the surface of the catalyst. The re-exchange of surface function groups to hydroxide groups may also result in a reduction in RHP, which is a consequence of a decrease in the sulfide/hydroxide ratio. (When the same catalyst was irradiated several times, it was often found that the initial increasing periods were similar for each illumination cycle, indicating that this change is reversible or rather leads to equilibrium.)

## 2.2. Photocatalytic Activity of $Zn_{0.75}Cd_{0.25}S$ Catalysts

According to several publications [21,29,34,35,39], sulfide catalysts were precipitated from N-based complexes ( $NH_3$  or ethylenediamine). The application of complexes as metal ion sources may decrease the driving force of the precipitation, and can highly influence the process of co-precipitation. Although HTT is another important step in the preparation of the catalyst, its real effect on the photoactivity of  $ZnS$ – $CdS$  has not been widely investigated. Therefore, these effects were also investigated in our work.

Three catalysts with different metal ion: $NH_3$  ratios were prepared. First, no  $NH_3$  was added during the precipitation (Cat-0N). In the second case, a stoichiometric amount of 25%  $NH_3$  solution ( $1.5\text{ cm}^3$ ) was added to the metal acetate solution (Cat-1N). In this procedure there was not enough  $NH_3$  to entirely dissolve the  $Cd(OH)_2$  and  $Zn(OH)_2$  precipitates before the addition of  $Na_2S$ . In the third case, enough  $NH_3$  solution was added ( $3.0\text{ cm}^3$ ) to dissolve all of the hydroxide precipitates (Cat-2N).

The hydrogen production efficiencies were studied on the three catalysts both before (the resulting catalysts are designated with “-0H” extension) and after HTT. The measured RHP values are shown in Figure 2. The catalyst prepared without the addition of ammonia and without HTT displayed a very low catalytic activity ( $16\text{ }\mu\text{mol/h}$ ). This value increased by more than 10 times when the co-precipitation was performed from ammine complexes, no matter whether the stoichiometric amount or excess of ammonia was applied. The results also clearly show that the HTT significantly enhanced the activity of all investigated catalysts, and the best catalytic activity was measured for the sample prepared from the ammine complex, using a stoichiometric amount of ammonia. Its RHP reached  $350\text{ }\mu\text{mol/h}$  ( $19.3\text{ mmol/g/h}$ ), which is one of the best published values for such systems, although these rates strongly depend on the light sources and geometrical arrangements.

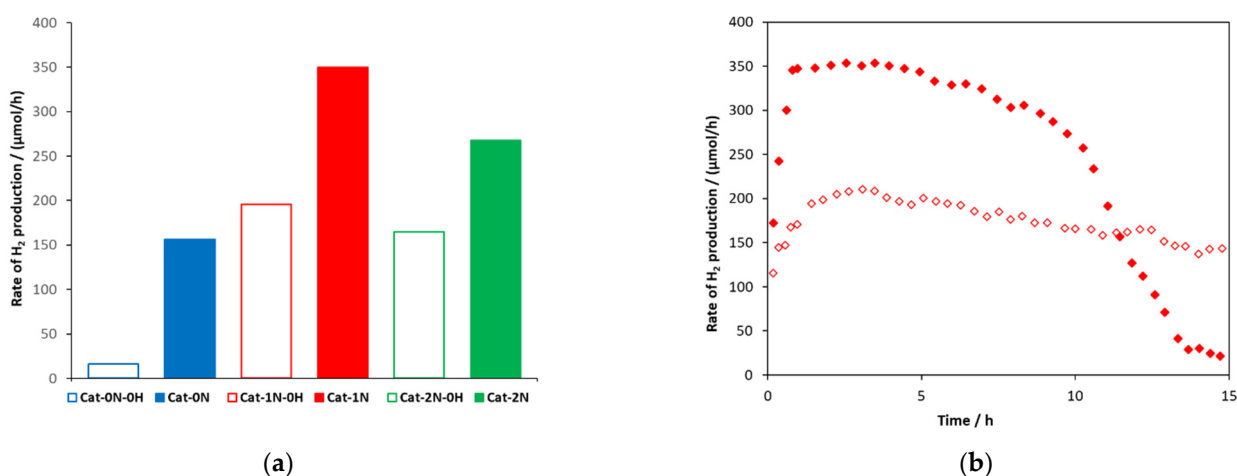


**Figure 2.** (a) Overall rate of  $H_2$  production for Cat-xN-(0H) before and after HTT (x: 0, 1, and 2) between 200 and 400 min, (b) overall rate of  $H_2$  production for Cat-1N before (-0H, empty marks) and after (filled marks) HTT as a function of time from a  $0.13\text{ M Na}_2\text{S}/0.18\text{ M Na}_2\text{SO}_3$  solution.

## 2.3. Diffuse Reflectance Spectra

The HTT of these catalysts caused a change in color from pale to dark yellow. This change is clearly shown by the diffuse reflectance spectra of the catalysts, from which the determinable band-gap (BG) value decreased only slightly, but the absolute value of the reflectance in the visible range significantly increased by the HTT (Figure 3 and Table 1). A decrease in BG of less than  $0.1\text{ eV}$  would only justify an increase in RHP of about 5–10% (see Figure S1), so there must also be some changes in the crystal structure that results in a shift of the conduction band (CB) towards a more negative potential or a decrease in the probability of electron–hole recombination.

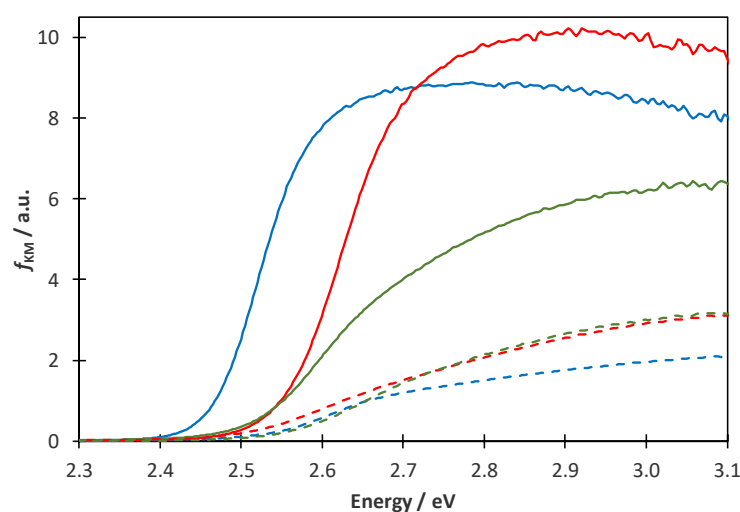


**Figure 3.** Kubelka-Munk functions of catalysts Cat-0N (solid blue), Cat-1N (solid red), Cat-2N (solid green), Cat-0N-0H (dashed blue), Cat-1N-0H (dashed red), and Cat-2N-0H (dashed green).

**Table 1.** The band-gap energies of different catalysts determined from Tauc-representation [40] of KM-functions (Figure S2).

Catalyst	Band-Gap Energy/eV	
	Before HTT	After HTT
Cat-0N	$2.58 \pm 0.03$	$2.50 \pm 0.02$
Cat-1N	$2.65 \pm 0.03$	$2.60 \pm 0.02$
Cat-2N	$2.65 \pm 0.03$	$2.57 \pm 0.02$

The BG and the CB potential of the  $\text{Cd}_{0.5}\text{Zn}_{0.5}\text{S}$  catalyst prepared from acetate salt and ethylenediamine (en) complexes were determined by electrochemical impedance spectroscopy by Chen et al. [21]. They found only a small difference in BG (2.39 eV and 2.36 eV), but the CB potential values differed significantly. The catalyst they prepared from a complex gave a much higher negative value ( $-1.06$  V) than that produced from acetate salts ( $-0.91$  V). Since the pH of the solution of sacrificial reagent in our system is approx. 13.5, a  $\text{H}_2/\text{H}^+$  redox potential of  $-0.8$  V or more negative is required for hydrogen evolution. Although the CB potentials were not measured in this work, according the results discussed above, a possible explanation of the higher RHP values in the case of catalysts prepared from ammine complexes are a result of the more negative Gibbs energy of hydrogen formation. Slower precipitation may result in a deviating crystal structure, the CB potential of which is different.

#### 2.4. XRD Pattern

In order to understand the previously described effects, X-ray diffraction (XRD) measurements were performed on samples dried from suspensions of the catalysts (Figure 4). Freshly prepared ZnS and CdS were used as references. From the diffractograms, it was clearly shown that all the ZnS–CdS samples consisted of only sulfides and did not contain any hydroxides or oxides traces. The investigated catalysts consist of cubic sphalerite and hawleyite. The latter has a crystal structure similar to that of sphalerite. Furthermore, the shifts at different peaks vary, which proves that it originates from the modification of the crystal structure. However, the position of the peaks, mainly the ones belonging to CdS, shifted towards higher  $2\theta$ , while those belonging to sphalerite slightly moved towards lower  $2\theta$ . This suggests that the  $\text{Zn}^{2+}$  ions are partly substituted by  $\text{Cd}^{2+}$  in the hawleyite lattice and the  $\text{Cd}^{2+}$  ions are slightly replaced by  $\text{Zn}^{2+}$  in the sphalerite lattice.

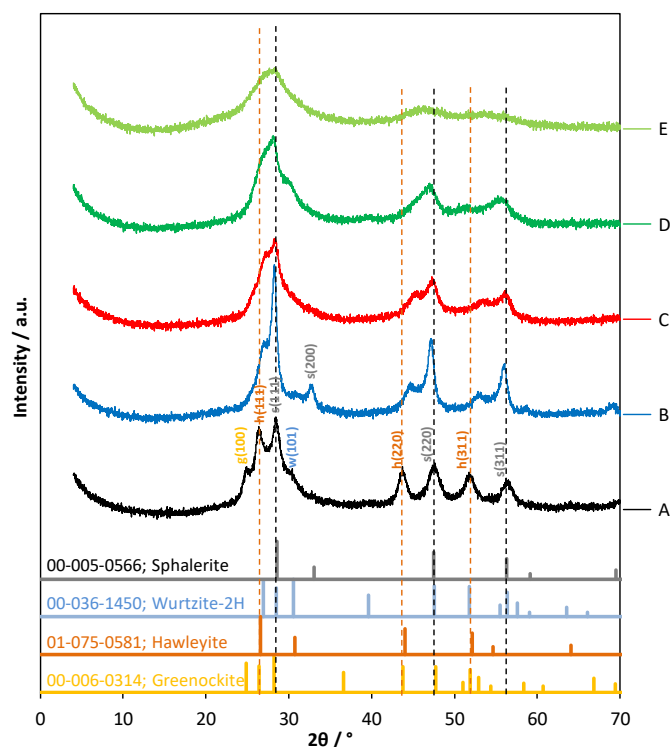


**Figure 4.** XRD patterns of photocatalysts: A: mixture of ZnS and CdS (in 3:1 molar ratio) synthesized and hydrothermally treated in the same way as other catalysts, B: Cat-0N, C: Cat-1N, D: Cat-2N, and E: Cat-2N-0H. The vertical lines designate the characteristic peaks of cubic sphalerite (gray) and hawleyite (red).

The XRD patterns of the catalyst prepared without adding any ammonia show only a slight shift of the peaks of hawleyite and sphalerite towards each other. The hawleyite peaks were shifted more than the sphalerite ones. Nevertheless, the peaks remained well separated. This sample also had the smallest full width at half maximum (FWHM) of the 111 reflection of sphalerite (at around  $28.559^\circ 2\theta$ ), i.e., the largest crystallite size (CS) according to the Scherrer equation, while the CS of hawleyite was the smallest one for this sample (Figure 5). The results suggest that if precipitation of CdS and ZnS does not occur from ammine complexes, both CdS and ZnS form faster than in the case of the precipitation from ammine complexes. Therefore, the  $Zn^{2+}$  ions are only slightly replaced by  $Cd^{2+}$  in sphalerite and, in turn, the  $Cd^{2+}$  ions by  $Zn^{2+}$  in hawleyite. However, the latter phenomenon may be more likely to occur due to the difference between the ionic radii. It is supported by the more perceptible shifts in the case of hawleyite. Increasing the amount of ammonia to the stoichiometric ratio, the 111 reflection of hawleyite (at around  $26.552^\circ 2\theta$ ) showed a larger shift and its calculated CS was very high. A further increase of the  $NH_3$  content resulted in a smaller CS of hawleyite and its 111 reflection appears only as a small shoulder. Although there was a large error in the determination of CS, a correlation between RHP and CS of hawleyite was observed for the examined catalysts (Figure 5).

Comparing the XRD pattern of hydrothermally treated and not treated catalysts, no visible change could be observed in the position of the peaks, but their FWHMs were decreased, i.e., the crystallite sizes increased, during the treatment. These changes suggest that the HTT favors the substitution of  $Cd^{2+}$  and  $Zn^{2+}$  ions for each other.

### 2.5. Equilibrium Calculations

Some equilibrium calculations were performed in order to evaluate the driving force during the preparation of the Cat-0N, Cat-1N, and Cat-2N catalysts. The driving force of the precipitation ( $\Delta\mu$ ) is the difference between the chemical potential of the reactants just mixed and that of the resulting suspension. This could be estimated from the supersatu-

ration ( $S$ ), which is equal to the ratio of the initial ( $c$ ) and the equilibrium free metal ion concentration ( $c^*$ ) [41].

$$\Delta\mu = RT \ln S = RT(\ln c - \ln c^*) \quad (1)$$

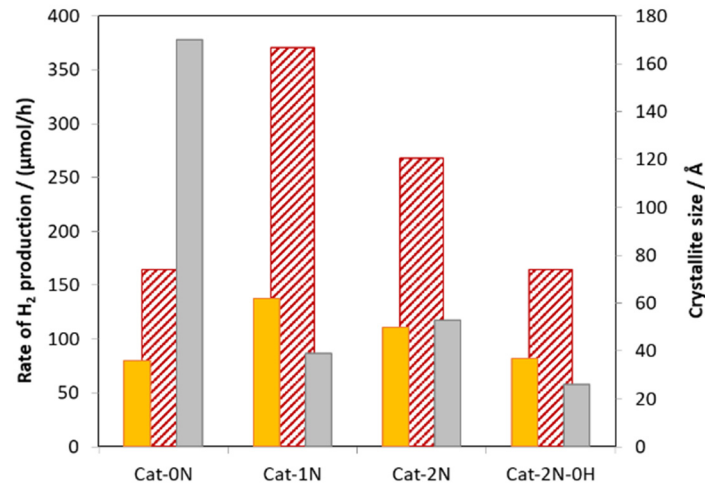


**Figure 5.** The overall rate of H<sub>2</sub> production (red cross-hatch) and the crystallite size of ZnS (grey) and CdS (orange) for the Cat-xN-(0H) catalysts (x: 0, 1, and 2).

The initial free metal ion concentration ( $c$ ) could be calculated from the stability constants of the ammine and hydroxo complexes and the protonation constants of ammonia and acetate ion (Table 2). The calculations were performed with a self-developed program using the Newton-Raphson method. The calculated free metal ion concentrations are indicated in Figure 6 by thin solid and dashed lines for the excess ( $T_{\text{NH}_3} = 3 \text{ M}$ ) or stoichiometric amount of ammonia ( $T_{\text{NH}_3} = 1.5 \text{ M}$ ), respectively. The orange and grey colors indicate the values for cadmium (II) and zinc (II) ions, respectively.

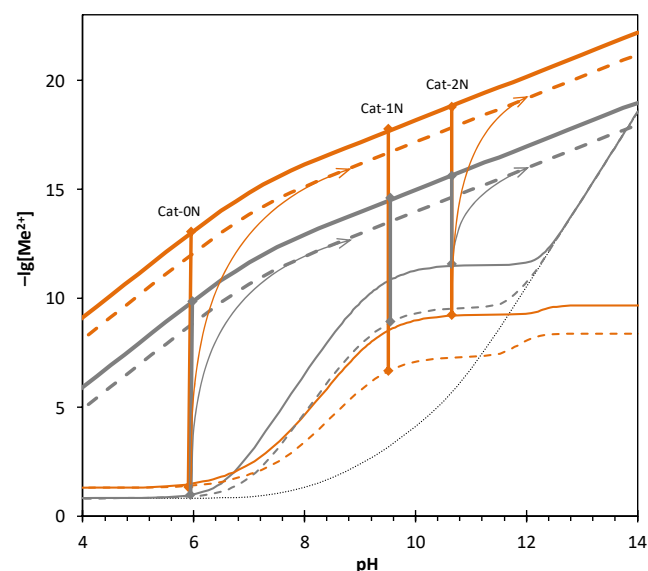


**Figure 6.** The calculated free Cd<sup>2+</sup> (orange) and Zn<sup>2+</sup> (grey) concentrations. The thin solid and dashed lines represent the values for 0.15 M total Zn<sup>2+</sup> and 0.05 M total Cd<sup>2+</sup> concentration for the excess ( $T_{\text{NH}_3} = 3 \text{ M}$ ) and stoichiometric amount of ammonia ( $T_{\text{NH}_3} = 1.5 \text{ M}$ ), respectively. The thick solid and dashed lines show the free equilibrium concentration at 0.22 M and 0.02 M total sulfide concentration, respectively. The thin dotted line shows the free Zn<sup>2+</sup> concentration, taking only the formation of hydroxo complex into account. For the meaning of the vertical lines and the arrows, see the text.

**Table 2.** Overall stability constants used for the calculation of the initial free metal ion concentrations [42,43].

n	NH <sub>4</sub> <sup>+</sup>	HAc	[Cd(NH <sub>3</sub> ) <sub>n</sub> ] <sup>2+</sup>	[Zn(NH <sub>3</sub> ) <sub>n</sub> ] <sup>2+</sup>	[Zn(OH) <sub>n</sub> ] <sup>2-n</sup>
1	9.25	4.73	2.51	2.32	6.31
2	-	-	4.47	4.61	11.19
3	-	-	5.77	6.97	14.31
4	-	-	6.56	9.36	17.7

Equilibrium metal ion concentrations ( $c^*$ ) at a given pH can be determined from the total concentration of sulfide ion in the solution ( $T_S$ ), the formation constants of CdS and ZnS ( $\lg K_{s,CdS} = 26.1$  and  $\lg K_{s,ZnS} = 22.9$  [44]) and the protonation constants of sulfide ion ( $\lg K_1 = 17.4$  and  $\lg K_2 = 7.05$  [45]).

$$c^* = \frac{1 + K_1[H^+] + K_1K_2[H^+]^2}{T_S K_s} \quad (2)$$

Two different  $c^*$  values have been calculated from two different total sulfide concentrations. The first was obtained assuming that all the added sulfides were still in dissolved form ( $T_S = 0.22$  M). The second one is for the state after the precipitation, when only the excess of the sulfide ion remains in solution ( $T_S = 0.02$  M). The former one is indicated by a thick solid line and the latter one by a thick dashed line in Figure 6.

Since the driving force of precipitation is proportional to  $(\ln c - \ln c^*)$ , the vertical distance between the  $\lg c$  and  $\lg c^*$  curves will also be proportional to the initial driving force, which was indicated by the thick vertical lines in Figure 6. The arrows indicate the real initial and end points before and after the addition of the sulfide reagent. In this figure, a higher lying curve represents a more stable species of a given metal ion.

The pH of the solution of cadmium acetate and zinc acetate was about 6.0, which increased to about 9 after the addition of a stoichiometric amount of Na<sub>2</sub>S, while the pH reached 12 with the application of 10% excess of sulfide reagent. If the precipitation was started from the solution containing stoichiometric amount or excess of ammonia, the initial pH was 9.6 or 10.5, which increased up to 12. Realizing the precipitation from complexes, the precipitation driving forces decreased in both cases, but this decrease was more enhanced for the formation of ZnS (Table 3). The lower driving force could cause a slower rate of precipitation, allowing the Cd<sup>2+</sup> and Zn<sup>2+</sup> ions to substitute each other, which is consistent with the peak shifts shown in XRD. The highest RHP of catalyst Cat-1N suggests that the undissolved Zn(OH)<sub>2</sub> particles influence the precipitation into a favorable direction.

**Table 3.** The initial pH of the solution of metal complexes before addition of Na<sub>2</sub>S reagent, and the initial supersaturation ( $c/c^*$ ) at the beginning of precipitation.

Catalyst	Cat-0N	Cat-1N	Cat-2N
pH	6.0	9.6	10.5
$\lg S_{ZnS}$	8.9	5.5	3.9
$\lg S_{CdS}$	11.7	10.9	9.4

## 2.6. SEM, TEM, and EDS Measurements

The SEM images of the catalysts measured with an energy dispersive detector clearly indicate their compositional inhomogeneity (Figure 7). All pictures show a darker (rich in ZnS) bulk with lighter (CdS-rich) spots. The Zn: Cd atomic ratios calculated by the EDS analysis were summarized in Table 4. The average atomic ratio for the whole photographed area were very close to the expected 3.0 value for all catalysts investigated. The catalyst



prepared without the addition of ammonia had a higher Zn:Cd ratio in the ZnS-rich bulk, and the number of CdS-rich particles were also higher than that for the other catalysts. Although the error of the calculated ratio is about 0.3–0.5, there is no doubt that the HTT enriches the CdS-rich particles in ZnS and the ZnS-rich particles in CdS, i.e., the sample becomes more homogeneous during the heat treatment. These results are in good agreement with the conclusions based on the XRD measurements and confirm the idea that  $\text{Cd}^{2+}$  and  $\text{Zn}^{2+}$  ions can substitute one other in the crystal lattice during HTT. In the case of the Cat-0N catalyst, the high initial chemical driving force could lead to the formation of numerous CdS cores, which caused the formation of many small CdS-rich particles.

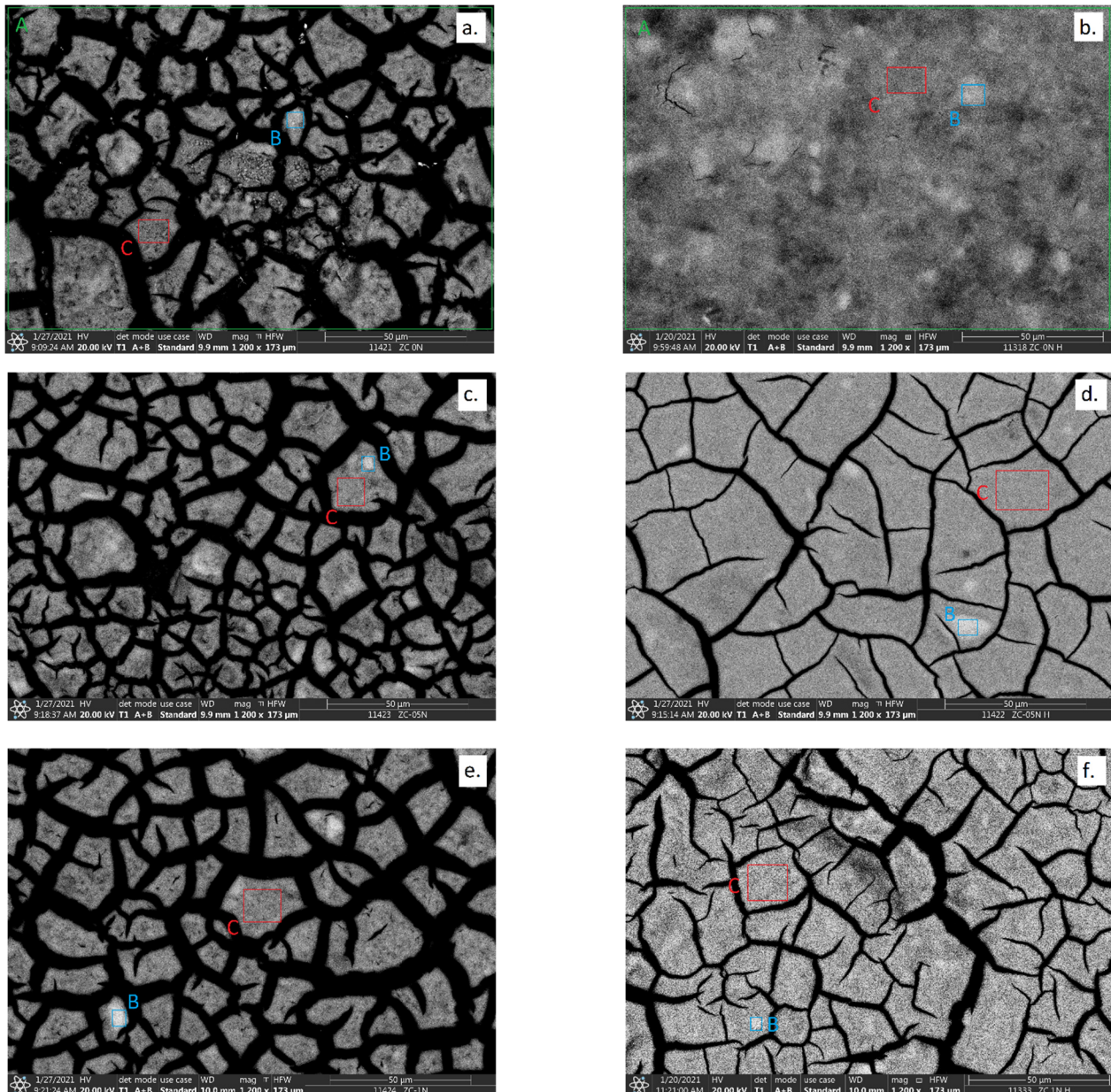


**Figure 7.** SEM images of Cat-0N-0H (a), Cat-0N (b), Cat-1N-0H (c), Cat-1N (d), Cat-2N-0H (e), and Cat-2N (f). The rectangles indicate the area analyzed by EDS. The “whole area” is not signed (by a green A) in the case of (c–f).

For the morphological study of the catalysts prepared from solutions of different ammonia contents, STEM measurements were carried out, the result of which are shown in Figure 8. Higher ammonia concentrations applied during preparation unambiguously decreased the particle size. In the case of the catalyst prepared in the absence of ammonia,

the size of the particles was in the region of about 10–40 nm (Figure 8a), and the shape of the particles were not elongated, i.e., nearly spherical. These results are in accordance with the XRD data (see Section 2.4), which showed the highest crystallite size in sphalerite. The large particle size may be one of the factors that decreased photocatalytic performance. Using ammonia, nanorods (or rather elongated nanoparticles) were formed with a typical diameter of 5–10 nm, and a length of 20–30 nm (Figure 8b). The particles prepared at the highest ammonia concentration were the smallest in size, 5–10 nm (Figure 8c).

**Table 4.** The Zn:Cd atomic ratios of the investigated catalysts calculated from the EDS analyses of different areas: A: average values regarding the whole area shown in the SEM pictures, B: the average of some lighter spots, and C: the average of a darker area.

Catalyst	Whole Average (A)	Lighter Spots (B)	Darker Area (C)
Cat-0N-0H	3.09	2.0	4.3
Cat-0N	3.14	2.5	3.4
Cat-1N-0H	3.10	1.3	3.6
Cat-1N	2.95	1.4	3.1
Cat-2N-0H	3.09	0.9	3.4
Cat-2N	3.02	1.3	3.1

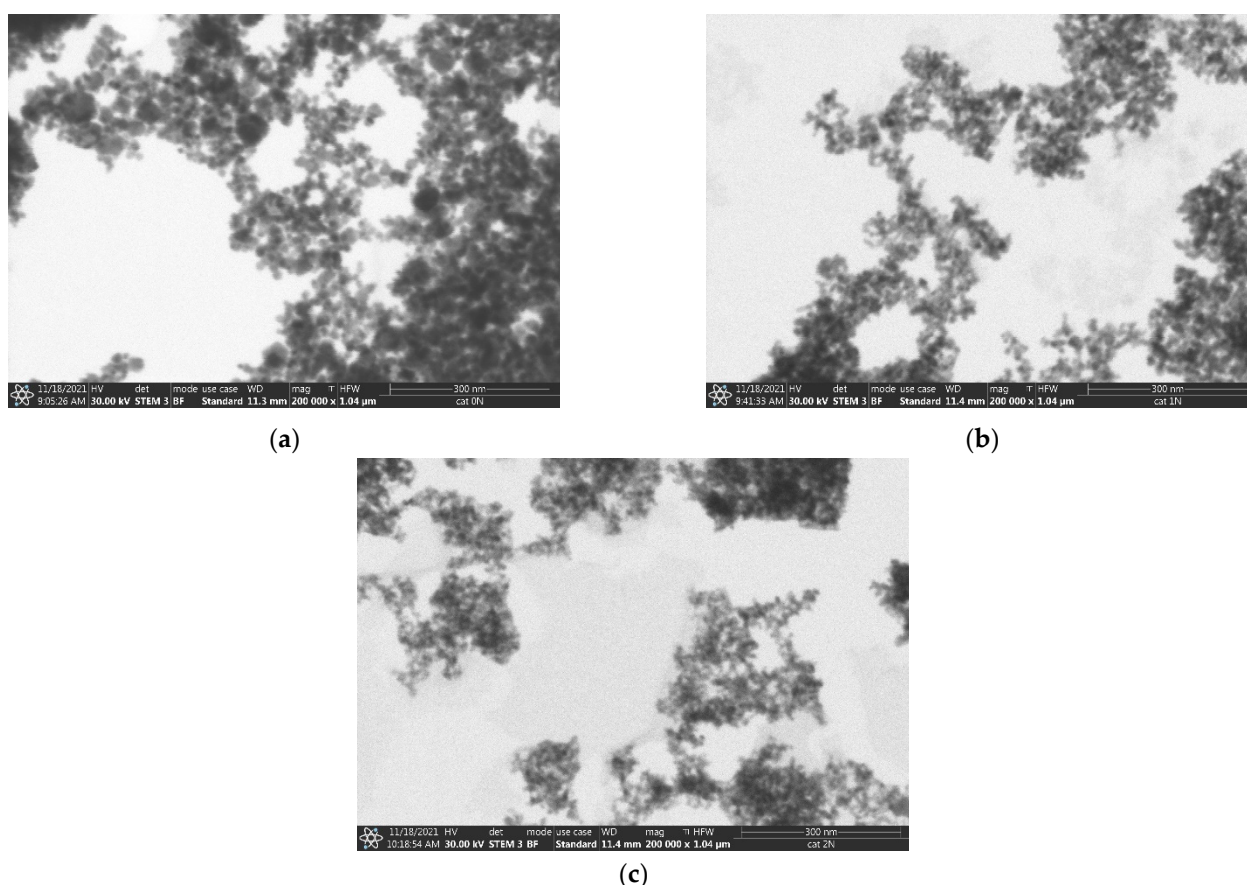


**Figure 8.** STEM images of Cat-0N (a), Cat-1N (b) and Cat-2N (c).

In order to understand the structural changes during HTT, a TEM analysis was performed before and after HTT for the Cat-1N sample (Figure 9). The two pairs of bright-field (Figure 9A,C) and HRTEM images (Figure 9E,G) show the differences in crystal sizes between the two samples; smaller crystals occur in Cat-1N-0H (Figure 9A,E),

whereas larger crystals are typical in the HTT sample (Figure 9C,G). According to the calculation of the crystal-size distribution (Figure S3), the typical size ranges are 3–12 nm and 5–26 nm, and the average sizes are around 5 nm and 12 nm in the Cat-1N-0H and Cat-1N samples, respectively. The crystal morphologies are similar in the two samples (axis ratios shown in Figure S3), and nearly isometric and slightly elongated shapes also occur in both samples. The crystal size difference is also recognizable in the electron diffraction patterns (Figure 9B,D), with broad diffraction rings produced by the Cat-1N-0H sample and sharp rings by the heat-treated sample, indicating smaller and larger average crystal sizes, respectively. These results are in agreement with the sizes obtained from XRD, likely due to the aging (Ostwald ripening) process during the treatment. The diffraction rings of both samples occur at the same *d*-values, close to the typical strong reflections of sphalerite.

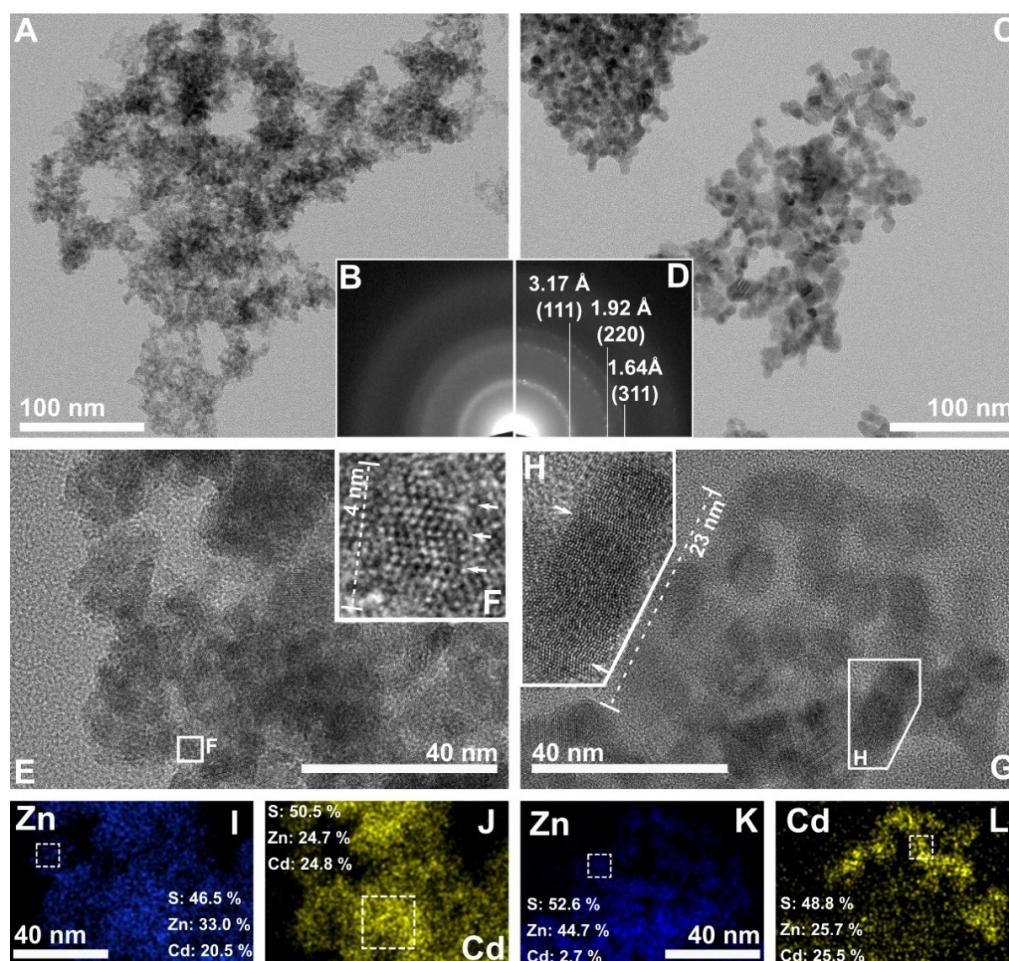


**Figure 9.** TEM/STEM results obtained from the Cat-1N-0H sample (left column, (A,B,E,F,I,J) images) and its heat-treated pair Cat-1N (right column, (C,D,G,H,K,L) images).

The compositional inhomogeneity of crystallites expected on the basis of SEM/EDS images is less obvious. The STEM EDS Zn (blue) and Cd (yellow) elemental maps were measured on the same areas as the HRTEM images (Figure 9E,G) and illustrate the inhomogeneity of the chemical compositions, as also indicated by the compositions calculated from the marked areas. For both catalysts, the Zn:Cd ratio varied over a wide range. Compared to the theoretical Zn:Cd ratio of 3:1, significant deviations in both directions were observed, but neither pure CdS, nor pure ZnS were detected in the STEM-EDS element maps. The nanocrystals with the highest Cd content had Zn:Cd ratios of around 1 (Figure 9J,L), whereas the most Zn-rich nanocrystals had at least 6–10% Cd content (Figure 9I,K). The elemental distribution within a given crystallite appeared to be uniform. Thus, a STEM-

EDS analysis suggested that the catalyst is composed of crystallites with homogeneous but variable compositions corresponding to a  $\text{Cd}_x\text{Zn}_{(1-x)}\text{S}$  solid solution. This result is consistent with the peak shifts observed in XRD measurements.

The structures of the two boxed crystals in Figure 9E,G (see the magnified inserts F and H) contain a series of stacking faults. Such defects occur in both samples but are more common in the hydrothermally treated one. Similar planar defects were also described in detail by Liu [35] and Chen et al. [21]. White arrows in Figure 9F,H clearly show twin boundaries in sphalerite, resulting in ABCABCACBA-type sequences of the close-packed layers, with the bold letter indicating a layer in a hcp stacking environment (as in wurtzite). In addition, stacking faults with ABCABCBCABC-type stacking sequences also occur, resulting in disordered structures between those of sphalerite and wurtzite (a common example is provided by the elongated nanocrystal in Figure 9H).

### 2.7. The Effect of the pH of Preparation on the ZnS–CdS Photoactivity

Three catalysts were prepared similarly to Cat-2N, but the initial pH was adjusted to 10.0, 11.0, or 12.0 through the addition of perchloric acid (2 M) after the formation of ammine complexes. The following procedure was identical with that applied for the other hydrothermally treated catalysts. The designation of the catalysts obtained were: Cat-2N-pH10, Cat-2N-pH11 and Cat-2N-pH12, corresponding to the initial pH applied for the preparation. The RHP was measured, and the results are depicted in Figure 10. Increasing the pH of the preparation in the presence of  $\text{NH}_4\text{OH}$  did not cause any remarkable changes in the evolution rate of hydrogen. This rate remained almost constant ( $\sim 260 \mu\text{mol/h}$ ) until the sulfide was depleted. This independence implies that, unlike the conventional preparation method, preparing the catalyst from ammine complexes confers the catalyst with high stability without the need of pH adjustment.

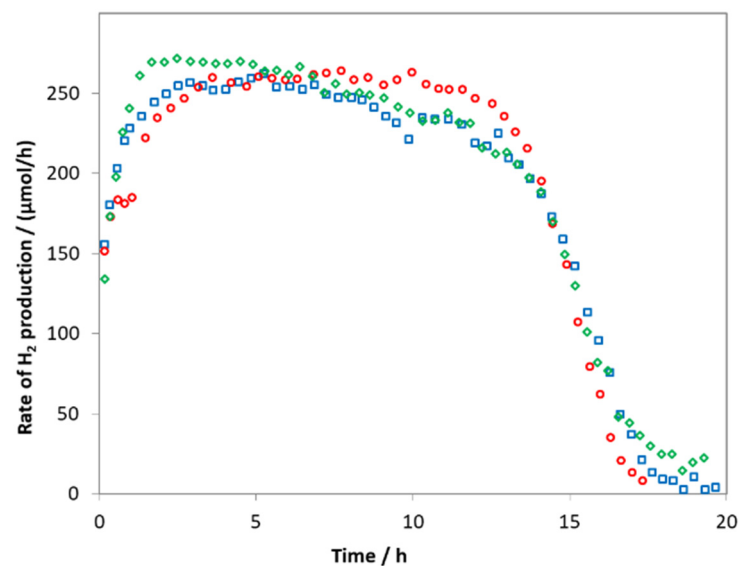


**Figure 10.** The rate of  $\text{H}_2$  production of Cat-2N-pH $x$  ( $x$ : 10 (blue  $\square$ ), 11 (red  $\circ$ ), and 12 (green  $\diamond$ )) as functions of time from a 0.13 M  $\text{Na}_2\text{S}$ /0.18 M  $\text{Na}_2\text{SO}_3$  solution.

### 2.8. Stability of ZnS–CdS Catalysts

The reusability of the ZnS–CdS catalysts with the highest RHP values was also studied in order to check their stability (Figure 11). The ZnS–CdS catalysts prepared with the stoichiometric amount and an excess of  $\text{NH}_4\text{OH}$  were re-illuminated for three cycles of 16 h each. The ZnS–CdS catalyst prepared with an excess of  $\text{NH}_4\text{OH}$  exhibited an appropriate stability, and only a small decrease in the RHP was observed after three illuminations (from  $270 \mu\text{mol/h}$  to  $240 \mu\text{mol/h}$ ). The catalyst prepared with the stoichiometric amount of  $\text{NH}_4\text{OH}$  appeared to be more stable than the previous one. Moreover, it demonstrated a

small increase during the second and third illuminations ( $\approx 390 \mu\text{mol/h}$ ), but the RHP in this case began decreasing after approximately 9 h, unlike the catalyst prepared with an excess of  $\text{NH}_4\text{OH}$  that showed a constant rate even after 13 h.

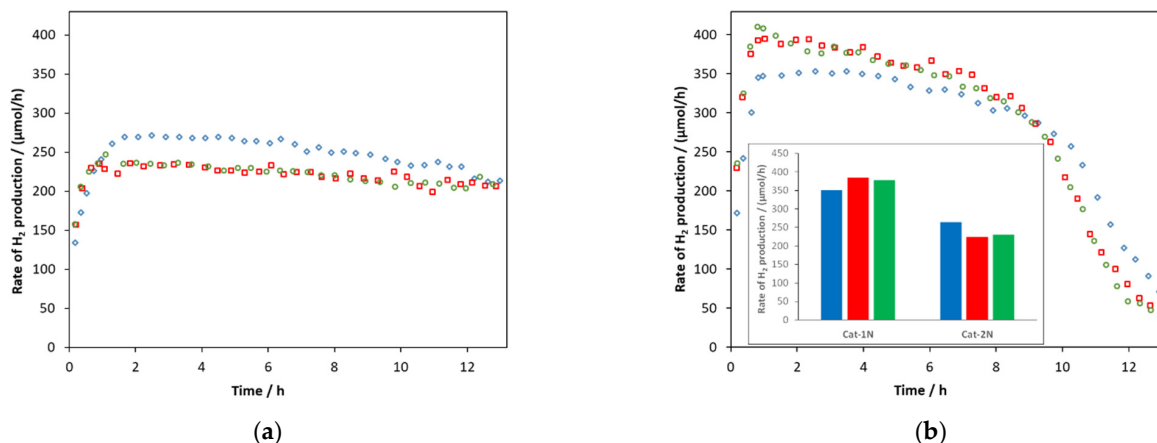


**Figure 11.** (a) The rate of H<sub>2</sub> production of Cat-2N for 3 cycles as a function of time from a 0.13M Na<sub>2</sub>S/0.18 M Na<sub>2</sub>SO<sub>3</sub> solution, (b) the rate of H<sub>2</sub> production of Cat-1N for 3 cycles as a function of time from a 0.13M Na<sub>2</sub>S/0.18M Na<sub>2</sub>SO<sub>3</sub> solution (inset: the overall rate of H<sub>2</sub> production of Cat-1N and Cat-2N for 3 cycles between 200 and 400 min). The blue, red, and green colors designate the 1st, 2nd, and 3rd illumination.

### 2.9. Quantum Yields

The quantum yields and the IPCEs (Incident-Photon-to-Current-Efficiency) were determined for the Cat-2N catalyst by three different light sources. The IPCEs and the quantum yields (QY) were calculated according to the following equations:

$$\text{IPCE} = \frac{2 \times \text{number of produced H}_2}{\text{number of incident photons}} \quad (3)$$

$$\text{QY} = \frac{2 \times \text{number of produced H}_2}{\text{number of absorbed photons}} \quad (4)$$

The number of incident photons were determined as described in the experimental part and in the Supplementary Materials, and the results are summarized in Table 5. The number of absorbed photons for opaque solids is difficult to calculate. Although it might be estimated from the DRS spectra, in this case the geometrical arrangement and the thickness of the catalyst layer were different, hence it was evaluated from the band gap. The number of the absorbed photons was calculated by supposing that all photons of higher energy than the band gap were absorbed. Of course, the value obtained in this way was higher than the actual value. In the case of illumination with the 380 nm LED, almost all photons were absorbed and the calculated IPCE and the QY were almost the same (9.2%). The IPCEs for the Hg-Xe lamp and for the visible LED were 6.8% and 1.9%, respectively.

**Table 5.** Measured data for the calculation of IPCE and QY for the Cat-2N catalyst illuminated by different light sources, and the resulting IPCE and QY values.

	Light Sources		
	UV-LED	Hg-Xe	Vis-LED
$n_{\text{photons}}/t$ (mmol/h)	12.06	11.25	27.75
RHP (mmol H <sub>2</sub> /h)	0.551	0.384	0.261
RHP (mmol H <sub>2</sub> /g/h)	30.6	21.3	14.5
IPCE	9.14%	6.82%	1.88%
Ratio of abs. photons	99.8%	85.0%	47.3%
QY	9.16%	8.02%	3.98%

Although the QY should be independent of the light source, our calculations resulted in lower QYs for these two light sources. Considering the shape of the Kubelka-Munk function of the catalyst, it can be seen that it increases from the band gap (2.57 eV) up to about 3.0 eV (Figure 12). When calculating the number of the absorbed photons, it was assumed that all photons in this range were absorbed, although the absorption increased from 0 to ~100% (see also the dashed lines in Figure 12). The relative intensity of the visible LED shows that all the emitted photons of this LED which have a higher energy than the BG fall into this range, so it is likely that only around 40% of the photons were absorbed in this range. In the case of the Hg-Xe lamp, there was only one peak in the growing region of the Kubelka-Munk function, hence, the difference between the calculated and the real absorbed fractions is lower (by only about 10%). The RHP values obtained with the three light sources are shown in Figure 13.

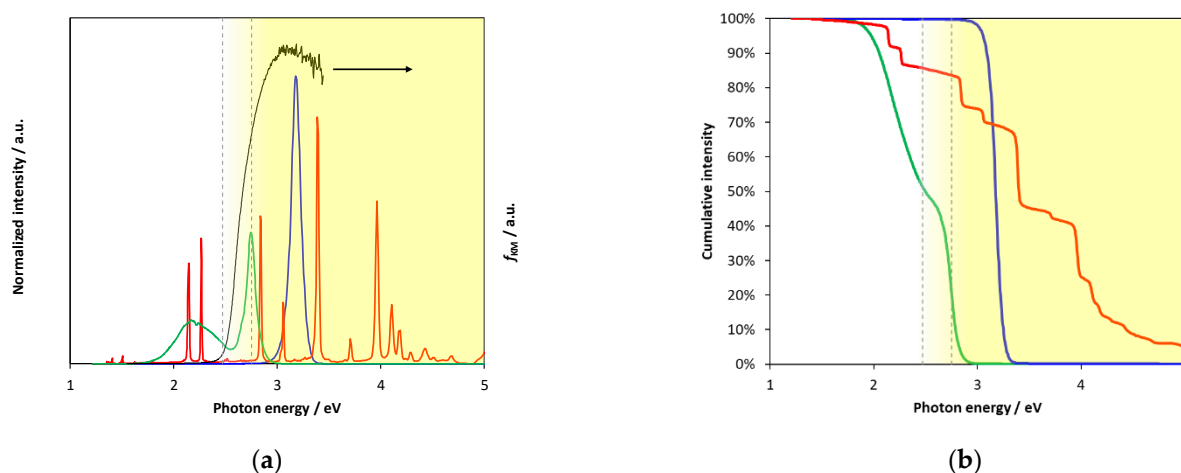


**Figure 12.** Normalized (a) and cumulative (b) intensity of the light sources applied for illumination (blue line: UV-LED, red: Hg-Xe arc lamp, green: vis LED). The emission spectra as functions of wavelength are also shown in the SM (Figure S4). The solid black line represent the KM-function, while the gray dashed lines indicate the intermediate energy range where the absorption steeply increases from the band gap for the Cat-2N catalyst. The yellow background symbolizes the light absorbed by the photocatalyst.

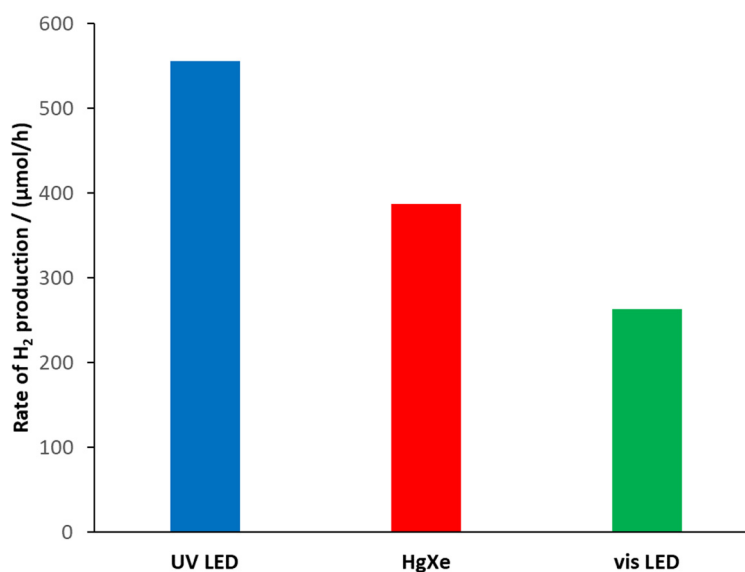


**Figure 13.** The overall rate of H<sub>2</sub> production for Cat-2N, using different light sources (vis LED, Xenon lamp, UV LED).

Since the geometric arrangements of all illumination experiments in this work were the same, the ratios of the RHPs to the QYs are equal (see in Figure S5). Based on this relationship, the QY of the most efficient Cat-1N catalyst was calculated to be 11.5% (see in Table S1).

Even if our goal was to study the effects of various conditions of the catalyst preparation on the efficiency of the photocatalytic hydrogen generation and not to reach a quantum yield approaching or exceeding the best quantum yields so far published, a comparison is worth making. The QY values obtained by similar systems for visible-light-driven hydrogen production are in the 1–62% range [16–18,23,30,35,39,46–50]. The order of magnitude of the best QY reached in our work corresponds to this range. Considering that the conditions of the photocatalysis were not optimized, e.g., no stirring was applied, and no precious co-catalyst was used, and the fraction of the toxic cadmium was rather low, this value may be promising for practical utilization.

### 3. Materials and Methods

#### 3.1. Materials

Zinc and cadmium acetate dihydrate ( $\text{Zn}(\text{CH}_3\text{COO})_2 \cdot 2\text{H}_2\text{O}$  and  $\text{Cd}(\text{CH}_3\text{COO})_2 \cdot 2\text{H}_2\text{O}$ ) and sodium thiosulfate pentahydrate ( $\text{Na}_2\text{S}_2\text{O}_3 \cdot 5\text{H}_2\text{O}$ ) were purchased from Reanal, and sodium sulfide nonahydrate >98% ( $\text{Na}_2\text{S} \cdot 9\text{H}_2\text{O}$ ) from Acros Organics. The water applied was cleaned by a Millipore Elix equipment (Millipore S.A.S., Molsheim, France) completed with a Milli-Q 50 purification system (Millipore S.A., Molsheim, France). The solutions containing sulfide/sulfite were prepared in advance using argon bubbled Milli-Q water and kept in the freezer for further experiments.

#### 3.2. Photocatalyst Preparation

The typical preparation method of ZnS–CdS catalyst was as follows: 1 mmol cadmium acetate dihydrate and 3 mmol zinc acetate dihydrate were dissolved in 10 mL Milli-Q water, 0, 1.5 mL or 3.0 mL of 25% ammonia solution was added, and the mixture was stirred for 5 min. 4.4 mmol (10% excess) of  $\text{Na}_2\text{S} \cdot 9\text{H}_2\text{O}$  was dissolved in 10 mL Milli-Q water which was de-aerated by bubbling argon gas for 20 min. This  $\text{Na}_2\text{S}$  solution was added to the solution containing the metal ions under vigorous stirring. The suspension was stirred for 10 min, and then poured into the 50 mL Teflon lined autoclave and treated at 170 °C for 3 h. After decantation, the yellowish ZnS–CdS precipitate was washed twice with Milli-Q water and centrifuged. The catalyst was then stored in water-suspension. In the case of pH-dependent investigation, the initial pH of the solution of metal-ammine complexes was set with 2M perchloric acid (pH = 10, 11, 12).

#### 3.3. Characterization

The crystallite size and phase composition was determined by an X-ray diffraction measurement (Philips PW3710, Cu  $K\alpha$  radiation, 50 kV and 40 mA). Data collections were carried out with X'Pert Data Collector software (2.0e, PANalytical B.V., Almelo, The Netherlands, 2010) The full width at half-maximum (FWHM) values of the individual reflections were determined by the profile fitting treatment of the X'Pert High Score Plus software (2.2.5, PANalytical B.V., Almelo, The Netherlands, 2009). The peak broadening caused by the samples was explained by the presence of very small crystallites. The broadening of the 111 reflections of hawleyite and sphalerite (measured breadth minus the instrumental breadth) was used to calculate the average crystallite size through the well-established Scherrer equation [51]. The FWHM of the 100 reflection of the ZnO (heated at 1000 °C) was employed as the instrumental breadth. The 01–075–0581, 00–005–0566, 00–006–0314, and 00–036–1450 Powder Diffraction File (PDF) of ICDD (International Centre for Diffraction Data) of hawleyite, sphalerite, greenockite, and wurtzite, respectively, were used to identify phases.

The morphology of the catalysts were studied by Schottky-field emission scanning electron microscope (FEI/Thermo Fisher Scientific, Waltham, MA, USA, model Apreo S)

under high vacuum conditions using scanning-transmission electron imaging (STEM) mode. The energy-dispersive-spectroscopy (EDS) studies were performed by an EDAX Ametek (Mahwah, NJ, USA) apparatus equipped with an Octane Elect Plus detector. Specord S600 spectrofluorometer (Analytic Jena GmbH, Jena, Germany) equipped with integrating sphere was used to measure the diffuse reflectance spectra and deduce the band-gap energy with the Kubelka-Munk function.

Samples for transmission electron microscopy (TEM) were prepared by depositing a drop of diluted aqueous suspension of the original samples on copper TEM grids that were covered by continuous carbon amorphous support film. TEM analyses were performed using a Talos F200X G2 instrument (Thermo Fisher Scientific), operated at 200 kV accelerating voltage, equipped with a field-emission gun and a four-detector Super-X energy-dispersive X-ray spectrometer (Thermo Fisher Scientific), and capable of working in both conventional TEM and scanning transmission (STEM) modes. In our study, TEM bright-field images, HRTEM images and STEM high-angle annular dark-field (HAADF) images were collected to visualize the crystal size and the morphology of the particles and HRTEM images, and electron diffraction patterns were used to study the structural properties. To characterize the size and the morphologies of the nanocrystals before and after HTT, around 100-100 particles were analyzed in both of the samples Cat-1N-0H and Cat-1N in the following way: Two dimensions (the longest and the perpendicular to the longest diameters) were measured on all particles with properly visible edges on each of the analyzed images (typically separated or slightly overlapping particles). To reach the required 100-100 particles, 5 and 6 HRTEM images were analyzed, resulting in 103 and 108 particles for the Cat-1N-0H and Cat-1N samples, respectively. STEM-EDS elemental mapping was applied to measure and visualize the chemical composition and inhomogeneities.

### 3.4. Photochemical Experiments

The photochemical experiments were performed under the conditions described by Fodor et al. [37], in a double-necked reactor of 40 cm<sup>3</sup> volume (14 mm height, 60 mm diameter). The total volume of all sacrificial solution was 30 cm<sup>3</sup> and they contained 0.13 M Na<sub>2</sub>S, 0.18 M Na<sub>2</sub>SO<sub>3</sub> and 18 mg of catalyst (0.6 g/dm<sup>3</sup>). Before illumination, all samples were de-aerated by argon bubbling for 10 min. Two 7 W 6000 K Optonica visible LEDs were used as the light source. The intensity of light sources (i.e., the amount of incident photons per unit volume per unit time) was determined by trioxalato-ferrate (III) actinometer. A detailed evaluation for this determination is described in the Supplementary Materials.

The evolved hydrogen was bubbled into a vessel filled with 1 mM NaOH solution and its volume was calculated from the mass of the displaced NaOH solution. Mass data were collected every minute using a Kern PCB balance (Kern & Sohn GmbH, Balingen, Germany) connected to a PC. In all cases, illuminations were performed until the end of the reactions. Importantly, the reaction mixture was not stirred during the irradiation. The amount of evolved hydrogen was equal to the initial amount of Na<sub>2</sub>S in all case.

## 4. Conclusions

In this work, ZnS-CdS composites were prepared in various ways, for visible-light-driven photocatalytic hydrogen generation in an aqueous system containing sulfide ions. The effect of their preparation conditions on the rate of hydrogen evolution was investigated. Our results unambiguously indicated that both the HTT of the catalysts and application of ammonia (as a ligand) during precipitation increased the photocatalytic efficiency. Notably, metal deposition on the catalyst particles was not required for promising photoactivity. Besides, the efficiency of these catalysts was independent of the pH applied for their preparation within the range of 10–12. This type of catalyst proved to be stable, i.e., its efficiency hardly changed during several re-uses. Additionally, the reaction mixture was not stirred during the irradiation, hence, this system is promising from the viewpoint of practical utilization.



**Supplementary Materials:** The following are available online at <https://www.mdpi.com/article/10.3390/catal11121534/s1>, Figure S1: Normalized (blue line) and cumulative (red line) intensity of the vis LED applied for illumination. The red dashed lines indicate the difference between the energies absorbed at 2.5 eV and 2.6 eV band gaps, Figure S2: Tauc representation of Cat-xN (solid lines in part „a”) and Cat-xN-0H (dashed lines in part „a” and solid lines in part „b” (blue: x = 0, red: x = 1, green x = 2)). Part „b” is the magnification of part „a” regarding Cat-xN-0H catalysts, Figure S3: Particle size distribution (longest diameter) and axis ratio distribution (longest diameter/perpendicular diameter) of the Cat-1N-0H sample (left diagrams) and Cat-1N sample (right diagrams) calculated from 103 and 108 particles, respectively, Figure S4: Normalized emission spectra of the light sources applied for illumination (blue line: UV-LED, red: Hg-Xe arc lamp, green: vis LED). The solid black line represents the KM-function, Figure S5: RHP of hydrothermally treated catalysts during illumination with vis LED (orange) and UV LED (violet) and the ratio of the RHPs measured with UV and vis LED, Table S1: Measured data for the calculation of IPCE and QY of Cat-xN catalysts illuminated by 50W UV-LED, and the resulting IPCE and QY values, Text S1: Determination of the intensity of light sources.

**Author Contributions:** Conceptualization, L.F.; methodology, L.F. and M.-A.M.; software, L.F. and M.-A.M.; validation, M.-A.M.; formal analysis, M.-A.M., É.M., M.J. and P.P.; investigation L.F. and M.-A.M.; resources, O.H.; data curation, M.-A.M., É.M., M.J., P.P. and L.F.; writing—original draft preparation, M.-A.M., L.F. and O.H.; writing—review and editing, O.H.; supervision, O.H. and L.F.; project administration, O.H.; funding acquisition, O.H. All authors have read and agreed to the published version of the manuscript.

**Funding:** Electron microscopy was performed in Nanolab of University of Pannonia, supported by the National Research, Development and Innovation Office under grant NKFIH-471-3/2021.

**Data Availability Statement:** The data presented in this study are available on request from the corresponding author. The data are not publicly available due to privacy.

**Acknowledgments:** The valuable advices of Mihály Pósfai for the interpretation of TEM images are gratefully acknowledged.

**Conflicts of Interest:** The authors declare no conflict of interest.

## References

1. Lewis, N.S. Toward Cost-Effective Solar Energy Use. *Science* **2007**, *315*, 798–801. [[CrossRef](#)]
2. Fujishima, A.; Honda, K. Electrochemical Photolysis of Water at a Semiconductor Electrode. *Nature* **1972**, *238*, 37–38. [[CrossRef](#)]
3. Baba, R.; Nakabayashi, S.; Fujishima, A.; Honda, K. Investigation of the mechanism of hydrogen evolution during photocatalytic water decomposition on metal-loaded semiconductor powders. *J. Phys. Chem.* **1985**, *89*, 1902–1905. [[CrossRef](#)]
4. Zhang, Y.; Heo, Y.-J.; Lee, J.-W.; Lee, J.-H.; Bajgai, J.; Lee, K.-J.; Park, S.-J. Photocatalytic Hydrogen Evolution via Water Splitting: A Short Review. *Catalysts* **2018**, *8*, 655. [[CrossRef](#)]
5. Tambwekar, S.V.; Subrahmanyam, M. Photocatalytic generation of hydrogen from hydrogen sulfide: An energy bargain. *Int. J. Hydrogen Energy* **1997**, *22*, 959–965. [[CrossRef](#)]
6. Kudo, A.; Miseki, Y. Heterogeneous photocatalyst materials for water splitting. *Chem. Soc. Rev.* **2009**, *38*, 253–278. [[CrossRef](#)]
7. Chen, X.; Shen, S.; Guo, L.; Mao, S.S. Semiconductor-based Photocatalytic Hydrogen Generation. *Chem. Rev.* **2010**, *110*, 6503–6570. [[CrossRef](#)]
8. Parida, K.M.; Mahanta, S.K.; Martha, S.; Nashim, A. Fabrication of NiO/Ta<sub>2</sub>O<sub>5</sub> composite photocatalyst for hydrogen production under visible light. *Int. J. Energy Res.* **2013**, *37*, 161–170. [[CrossRef](#)]
9. Ramírez-Ortega, D.; Guerrero-Araque, D.; Acevedo-Peña, P.; Reguera, E.; Calderon, H.A.; Zanella, R. Enhancing the photocatalytic hydrogen production of the ZnO–TiO<sub>2</sub> heterojunction by supporting nanoscale Au islands. *Int. J. Hydrogen Energy* **2021**, *46*, 34333. [[CrossRef](#)]
10. Machín, A.; Cotto, M.; Duconge, J.; Arango, J.C.; Morant, C.; Pinilla, S.; Soto-Vázquez, L.; Resto, E.; Márquez, F. Hydrogen production via water splitting using different Au@ZnO catalysts under UV–vis irradiation. *J. Photochem. Photobiol. A Chem.* **2018**, *353*, 385–394. [[CrossRef](#)]
11. Lu, G.; Li, S. Hydrogen production by H<sub>2</sub>S photodecomposition on ZnFe<sub>2</sub>O<sub>4</sub> catalyst. *Int. J. Hydrogen Energy* **1992**, *17*, 767–770. [[CrossRef](#)]
12. Zhang, K.; Guo, L. Metal sulphide semiconductors for photocatalytic hydrogen production. *Catal. Sci. Technol.* **2013**, *3*, 1672. [[CrossRef](#)]
13. Raevskaya, A.E.; Stroyuk, A.L.; Kryukov, A.I.; Kuchmii, S.Y. Structural and optical characteristics of Cd<sub>x</sub>Zn<sub>1-x</sub>S nanoparticles stabilized in aqueous solutions of polymers. *Theor. Exp. Chem.* **2006**, *42*, 181–185. [[CrossRef](#)]

14. Akinwunmi, O.O.; Egharevba, G.O.; Ajayi, E.O.B. Synthesis and Characterization of CdS, ZnS and CdZnS Nanoparticles Embedded in Polystyrene. *J. Mod. Phys.* **2014**, *05*, 257–266. [[CrossRef](#)]
15. Preethi, V.; Kanmani, S. Photocatalytic hydrogen production using Fe<sub>2</sub>O<sub>3</sub>-based core shell nano particles with ZnS and CdS. *Int. J. Hydrogen Energy* **2014**, *39*, 1613–1622. [[CrossRef](#)]
16. Zhang, W.; Zhong, Z.; Wang, Y.; Xu, R. Doped Solid Solution: (Zn<sub>0.95</sub>Cu<sub>0.05</sub>)<sub>1-x</sub>Cd<sub>x</sub> Nanocrystals with High Activity for H<sub>2</sub> Evolution from Aqueous Solutions under Visible Light. *J. Phys. Chem. C* **2008**, *112*, 17635–17642. [[CrossRef](#)]
17. Stroyuk, A.L.; Raevskaya, A.E.; Korzhak, A.V.; Kotenko, I.E.; Glebov, E.M.; Plyusnin, V.F.; Kuchmii, S.Y. Photocatalytic production of hydrogen in systems based on Cd<sub>x</sub>Zn<sub>1-x</sub>S/Ni<sup>0</sup> nanostructures. *Theor. Exp. Chem.* **2009**, *45*, 12–22. [[CrossRef](#)]
18. Li, N.; Zhou, B.; Guo, P.; Zhou, J.; Jing, D. Fabrication of noble-metal-free Cd<sub>0.5</sub>Zn<sub>0.5</sub>S/NiS hybrid photocatalyst for efficient solar hydrogen evolution. *Int. J. Hydrogen Energy* **2013**, *38*, 11268–11277. [[CrossRef](#)]
19. Villa, K.; Domènech, X.; García-Pérez, U.M.; Peral, J. Optimization of the experimental conditions of hydrogen production by the Pt-(CdS/ZnS) system under visible light illumination. *RSC Adv.* **2016**, *6*, 36681–36688. [[CrossRef](#)]
20. Wang, J.; Li, B.; Chen, J.; Li, N.; Zheng, J.; Zhao, J.; Zhu, Z. Enhanced photocatalytic H<sub>2</sub>-production activity of Cd<sub>x</sub>Zn<sub>1-x</sub>S nanocrystals by surface loading MS (M=Ni, Co, Cu) species. *Appl. Surf. Sci.* **2012**, *259*, 118–123. [[CrossRef](#)]
21. Chen, M.; Wu, P.; Zhu, Y.; Yang, S.; Lu, Y.; Lin, Z. Enhanced photocatalytic H<sub>2</sub> production activity of CdZnS with stacking faults structure assisted by ethylenediamine and NiS. *Int. J. Hydrogen Energy* **2018**, *43*, 10938–10949. [[CrossRef](#)]
22. Villoria, J.A.; Navarro Yerga, R.M.; Al-Zahrani, S.M.; Fierro, J.L.G. Photocatalytic Hydrogen Production on Cd<sub>1-x</sub>Zn<sub>x</sub>S Solid Solutions under Visible Light: Influence of Thermal Treatment. *Ind. Eng. Chem. Res.* **2010**, *49*, 6854–6861. [[CrossRef](#)]
23. Chen, Y.; Guo, L. Highly efficient visible-light-driven photocatalytic hydrogen production from water using Cd<sub>0.5</sub>Zn<sub>0.5</sub>S/TNTs (titanate nanotubes) nanocomposites without noble metals. *J. Mater. Chem.* **2012**, *22*, 7507. [[CrossRef](#)]
24. Xiang, J.; Wang, H.; Wang, X.; Chen, X.; Wu, T.; Wan, H.; Liu, Y.; Wang, H. Colloidal Cd<sub>x</sub>Zn<sub>1-x</sub>S nanocrystals as efficient photocatalysts for H<sub>2</sub> production under visible-light irradiation. *RSC Adv.* **2019**, *9*, 4001–4007. [[CrossRef](#)]
25. Koca, A.; Sahin, M. Photocatalytic hydrogen production by direct sun light from sulfide/sulfite solution. *Int. J. Hydrogen Energy* **2002**, *27*, 363–367. [[CrossRef](#)]
26. Chan, C.-C.; Chang, C.-C.; Hsu, C.-H.; Weng, Y.-C.; Chen, K.-Y.; Lin, H.-H.; Huang, W.-C.; Cheng, S.-F. Efficient and stable photocatalytic hydrogen production from water splitting over Zn<sub>x</sub>Cd<sub>1-x</sub>S solid solutions under visible light irradiation. *Int. J. Hydrogen Energy* **2014**, *39*, 1630–1639. [[CrossRef](#)]
27. Kundu, J.; Mal, D.D.; Pradhan, D. Single-step solvothermal synthesis of highly uniform Cd<sub>x</sub>Zn<sub>1-x</sub>S nanospheres for improved visible light photocatalytic hydrogen generation. *Inorg. Chem. Front.* **2021**, *8*, 3055–3065. [[CrossRef](#)]
28. Li, Q.; Meng, H.; Zhou, P.; Zheng, Y.; Wang, J.; Yu, J.; Gong, J. Zn<sub>1-x</sub>Cd<sub>x</sub>S Solid Solutions with Controlled Bandgap and Enhanced Visible-Light Photocatalytic H<sub>2</sub>-Production Activity. *ACS Catal.* **2013**, *3*, 882–889. [[CrossRef](#)]
29. Ali, A.H.; Jassem, S.A. Preparation and Study of CdS thin films at different concentration thiorea by chemical bath deposition (CBD) method. *World Sci. News* **2015**, *23*, 73–89.
30. Zhang, Y.; Peng, Z.; Guan, S.; Fu, X. Novel β-NiS film modified CdS nanoflowers heterostructure nanocomposite: Extraordinarily highly efficient photocatalysts for hydrogen evolution. *Appl. Catal. B Environ.* **2018**, *224*, 1000–1008. [[CrossRef](#)]
31. Liu, X.; Liang, X.; Wang, P.; Huang, B.; Qin, X.; Zhang, X.; Dai, Y. Highly efficient and noble metal-free NiS modified Mn<sub>x</sub>Cd<sub>1-x</sub>S solid solutions with enhanced photocatalytic activity for hydrogen evolution under visible light irradiation. *Appl. Catal. B Environ.* **2017**, *203*, 282–288. [[CrossRef](#)]
32. Mintcheva, N.; Gicheva, G.; Panayotova, M.; Wunderlich, W.; Kuchmizhak, A.A.; Kulinich, S.A. Preparation and Photocatalytic Properties of CdS and ZnS Nanomaterials Derived from Metal Xanthate. *Materials* **2019**, *12*, 3313. [[CrossRef](#)]
33. González-Panzo, I.J.; Martín-Vázquez, P.E.; Oliva, A.I. Physicochemical Conditions for ZnS Films Deposited by Chemical Bath. *J. Electrochem. Soc.* **2014**, *161*, D181–D189. [[CrossRef](#)]
34. Qin, Z.; Xue, F.; Chen, Y.; Shen, S.; Guo, L. Spatial charge separation of one-dimensional Ni<sub>2</sub>P-Cd<sub>0.9</sub>Zn<sub>0.1</sub>S/g-C<sub>3</sub>N<sub>4</sub> heterostructure for high-quantum-yield photocatalytic hydrogen production. *Appl. Catal. B Environ.* **2017**, *217*, 551–559. [[CrossRef](#)]
35. Liu, M.; Jing, D.; Zhou, Z.; Guo, L. Twin-induced one-dimensional homojunctions yield high quantum efficiency for solar hydrogen generation. *Nat. Commun.* **2013**, *4*, 2278. [[CrossRef](#)]
36. Zhong, W.; Huang, Y.; Wang, X.; Fan, J.; Yu, H. Colloidal CdS and CdZnS nanocrystal photocatalysts with massive S<sup>2-</sup>-adsorption: One-step facile synthesis and highly efficient H<sub>2</sub>-evolution performance. *Chem. Commun.* **2020**, *56*, 9316–9319. [[CrossRef](#)]
37. Fodor, L.; Solymosi, B.; Horváth, O. Investigation of Hydrogen Production from Alkaline Sulfide Solution with Nanosized CdS/ZnS-PdS Photocatalyst of Various Compositions. *J. Nanosci. Nanotechnol.* **2019**, *19*, 509–515. [[CrossRef](#)]
38. Guo, X.; Chen, Y.; Qin, Z.; Wang, M.; Guo, L. One-step hydrothermal synthesis of Zn<sub>x</sub>Cd<sub>1-x</sub>S/ZnO heterostructures for efficient photocatalytic hydrogen production. *Int. J. Hydrogen Energy* **2016**, *41*, 15208–15217. [[CrossRef](#)]
39. He, K.; Guo, L. NiS modified CdS pyramids with stacking fault structures: Highly efficient and stable photocatalysts for hydrogen production from water. *Int. J. Hydrogen Energy* **2017**, *42*, 23995–24005. [[CrossRef](#)]
40. Tauc, J.; Grigorovici, R.; Vancu, A. Optical Properties and Electronic Structure of Amorphous Germanium. *Phys. Status Solidi* **1966**, *15*, 627–637. [[CrossRef](#)]
41. Mullin, J.W. *Crystallisation*; Butterworth Heinemann: Oxford, UK, 2001.
42. Sillen, L.G. *Stability Constants of Metal Ion Complexes, Part I: Inorganic Ligands, Special Publication (RSC) No. 17*; Chemical Society: London, UK, 1964.

43. Martell, A.E. *Stability Constants of Metal Ion Complexes, Part II: Organic Ligands, Special Publication (RSC) No. 17*; Chemical Society: London, UK, 1964.
44. Högfeldt, E. *Stability Constants of Metal-Ion Complexes, Part A: Inorganic Ligands, International Union of Pure and Applied Chemistry: IUPAC Chemical Data Series, No. 21*; Pergamon Press: Oxford, UK, 1982.
45. Migdisov, A.A.; Williams-Jones, A.E.; Lakshtanov, L.Z.; Alekhin, Y.V. Estimates of the second dissociation constant of H<sub>2</sub>S from the surface sulfidation of crystalline sulfur. *Geochim. Cosmochim. Acta* **2002**, *66*, 1713–1725. [[CrossRef](#)]
46. Xing, C.; Zhang, Y.; Yan, W.; Guo, L. Band structure-controlled solid solution of Cd<sub>1-x</sub>Zn<sub>x</sub>S photocatalyst for hydrogen production by water splitting. *Int. J. Hydrogen Energy* **2006**, *31*, 2018–2024. [[CrossRef](#)]
47. Kozlova, E.A.; Markovskaya, D.V.; Cherepanova, S.V.; Saraev, A.A.; Gerasimov, E.Y.; Perevalov, T.V.; Kaichev, V.V.; Parmon, V.N. Novel photocatalysts based on Cd<sub>1-x</sub>Zn<sub>x</sub>S/Zn(OH)<sub>2</sub> for the hydrogen evolution from water solutions of ethanol. *Int. J. Hydrogen Energy* **2014**, *39*, 18758–18769. [[CrossRef](#)]
48. Wang, X.; Shih, K.; Li, X.Y. Photocatalytic hydrogen generation from water under visible light using core/shell nano-catalysts. *Water Sci. Technol.* **2010**, *61*, 2303–2308. [[CrossRef](#)]
49. Lyubina, T.P.; Kozlova, E.A. New photocatalysts based on cadmium and zinc sulfides for hydrogen evolution from aqueous Na<sub>2</sub>S-Na<sub>2</sub>SO<sub>3</sub> solutions under irradiation with visible light. *Kinet. Catal.* **2012**, *53*, 188–196. [[CrossRef](#)]
50. Li, X.; Xue, F.; Li, N.; Wei, X.; Liu, H.; Zhou, J.; Lyu, B.; Liu, M. One-Pot Hydrothermal Synthesis of MoS<sub>2</sub>/Zn<sub>0.5</sub>Cd<sub>0.5</sub>S Heterojunction for Enhanced Photocatalytic H<sub>2</sub> Production. *Front. Chem.* **2020**, *8*, 779. [[CrossRef](#)]
51. Bish, D.L.; Post, J.E. *Modern Powder Diffraction*; The Mineralogical Society of America: Washington, DC, USA, 1989.